Enhancing the Resistive Memory Window through Band Gap Tuning in Solid Solution (Cr1–xVx)2O3

Michael Rodriguez-Fano, Mohamad Haydoura, Julien Tranchant, Etienne Janod, Benoît Corraze, Pierre-Yves Jouan, Laurent Cario, Marie-Paule Besland

Enhancing the resistive memory window through band gap tuning in the solid solution $(Cr_{1-x}V_x)_2O_3$

Michael Rodriguez-Fano, Mohamad Haydoura, Julien Tranchant, Etienne Janod, Benoît Corraze, Pierre-Yves Jouan, Laurent Cario and Marie-Paule Besland**

Université de Nantes, CNRS, Institut des Matériaux Jean Rouxel, IMN, F-44000 Nantes, France

* marie-paule.besland@cnrs-imn.fr, julien.tranchant@cnrs-imn.fr

ABSTRACT: *Memories based on the Insulator-to-metal transition in correlated insulators are promising to overcome the limitations of alternative non-volatile memory technologies. However, associated performances have been demonstrated so far only on narrow gap compounds, such as* $(V_{0.95}Cr_{0.05})_2O_3$ *, displaying a tight memory window. In the present study, V-substituted* Cr_2O_3 *compounds* $(Cr_{1-x}V_x)_2O_3$ *have been synthesized and widely investigated in thin films, single crystals and polycrystalline powders, for the whole range of chemical composition (*$0<x<1$*). Physico-chemical, structural and optical properties of the annealed magnetron sputtered thin films are in very good agreement with those of polycrystalline powders. Indeed all compounds exhibit the same crystalline structure with a cell parameters evolution consistent with a solid solution over the whole range of x values, as demonstrated by X-Ray Diffraction and Raman scattering. Moreover, the optical band gap of V-substituted* Cr_2O_3 *compounds decreases from 3 eV for* Cr_2O_3 *to 0 eV for* V_2O_3*. In the same way, the resistivity is decreased by almost five order of magnitude as the V content x is varying from 0 to 1, similarly in thin films and single crystals. Finally, a reversible resistive switching has been observed for thin films of three selected V content (*$x=0.30$*, 0.70 and 0.95). Resistive switching performed on MIM devices based on a 50 nm thick* $(Cr_{0.30}V_{0.70})_2O_3$ *thin film show a high endurance of 1000 resistive switching cycles and a memory window* R_{OFF}/R_{ON} *higher by three orders of magnitude, as compared to* $(Cr_{0.05}V_{0.95})_2O_3$*. This comprehensive study demonstrates that a large range of memory window can be reached by tuning the band gap while varying the V content in the* $(Cr_{1-x}V_x)_2O_3$ *solid solution. It thus confirms the potential of correlated insulators for memory applications.*

KEYWORDS. V-substituted Cr_2O_3, solid solution, band gap, resistive switching, non-volatile memory.

INTRODUCTION

In the last decade, the miniaturization of Flash memories has been slowing down and toils to fulfill the ever-increasing needs for reliable data storage. In this framework, 3D stacking has been proposed as a solution but drastically increases the cost of fabrication[1] by the addition of numerous lithographic steps. In addition, the reliability of data storage declines progressively for the latest technology nodes, now below 10 nm, because of increasing leakage currents and need for counteracting expensive technological solutions[2].

In that respect, many researches have been and are still dedicated to alternative technologies to face the storage requirements. Numerous studies address the development of alternative technologies: Magnetic Random Access Memory (MRAM), Phase Change Memory (PCRAM), Ferroelectric Memory (FeRAM) and Resistive Memory (ReRAM). These technologies offer attractive characteristics as programming time in the ns range, writing energy below 10^{-11} J/bit, cell size promising to be smaller than Flash memory and are compatible with integration in a CMOS technology. Nevertheless, in all these alternatives important shortcomings are still limiting their industrial reliability[3,4]. PCRAM faces high current consumption[5], FeRAM has large three-dimensional structures (> 100 nm) limiting so far the storage density[6], MRAM suffers from low memory window and weak thermal stability [7,8], and oxide based ReRAMs (OxRAMs) display high variability of its resistance states, directly linked to their working principle[9].

This work focuses on a different type of ReRAM, based on Correlated Insulators. The insulating state of these compounds is characterized by the localization of the valence electrons submitted to a strong electron-electron repulsion[10]. Previous works on resistive switching in such compounds have highlighted the interest of Mott insulators for non-volatile memory applications[11].

More specifically, our works have shown that the application of an electric pulse on a narrow gap Mott insulator triggers an avalanche breakdown above a threshold electric field[12,13]. For sufficient electric field, a non-volatile granular conductive filament is created in which the lattice is compressed[9]. Owing to the physics of Mott insulators, this compressed filament is much more conductive than the pristine material and accounts for the observed Insulator-to-Metal Transition (IMT). This resistive switching behavior of electronic nature is reversible since the application of another electric pulse can induce a switch back to the pristine state by self-Joule heating of the filament [14]. The application of an appropriate pulse sequence thus enables to switch back and forth between high (pristine value) and low resistive states. This mechanism was demonstrated first in single crystals[15] and further in thin layers of two materials, GaV_4S_8[16] and $(Cr_{0.05}V_{0.95})_2O_3$[17]. Moreover, we demonstrated that it is actually universal to all Mott insulators[9]. It does not involve any atom migration[18] nor forming step[9], which differentiates it strongly from mechanisms based on ionic electro-migration commonly used to explain IMT in oxides[7], or interfacial switching observed in PCMOs[19].

Based on this specific physical mechanism, resistive switching was demonstrated (*i.e.* stable resistance states, scalability down to 30 nm, and write current < 50 μA) [20,16]. These features of Mott memories make them promising to overcome the limitations of alternative non-volatile memory technologies. However, only compounds with narrow band gap, *i.e.* namely 0.3 eV and 0.15 eV for GaV_4S_8 and $(Cr_{0.05}V_{0.95})_2O_3$ respectively[10,11], have been investigated so far, yielding limited memory window due to their pristine resistivity in the 1-10 Ω.cm range. On the other hand, these previous works suggest an enhancement of the memory window when the gap value increases, which enables to envision Mott memories with high R_{OFF}/R_{ON} ratios, based on large gap

correlated insulators. However, to date no work in literature explored deeply the resistive switching (RS) in large gap correlated insulators and the impact of the gap value on the memory window.

Here we show that thin films of the family of correlated insulators $(Cr_{1-x}V_x)_2O_3$ have a band gap that can be tuned in the 0-3 eV range, with the possibility of resistive switching cycling. In this extensive original study of structural, optical and electrical properties of V-substituted Cr_2O_3 material, the chemical composition has been varied in a large extent for $0 < x < 1$. To get reliable references, single crystals and powders were first elaborated and characterized. In a second step, thin films have been obtained by magnetron co-sputtering of two metallic targets (Vanadium and Chromium). An annealing step under controlled oxygen pressure enabled to obtain well-crystallized and stoichiometric V-substituted Cr_2O_3 thin films. The impact of the variation of the V content on the crystalline structure, band gap value and transport properties has been investigated. Finally, resistive switching experiments were performed on some selected miniaturized devices based on $(Cr_{1-x}V_x)_2O_3$ thin films and demonstrated for the first time the enhancement of the memory window as the band gap increases within this solid solution of narrow to large band gap correlated insulators.

EXPERIMENTAL SECTION

Synthesis of powders and single-crystals

$(Cr_{1-x}V_x)_2O_3$ powder samples with various "x" Vanadium contents were prepared using liquid-phase syntheses. Ammonium metavanadate NH_4VO_3, Chromic Nitrate nonahydrate $Cr(NO_3)_3$, $9H_2O$ and Citric acid $C_6H_8O_7$ were first dissolved together in 100 ml of distilled water following the reaction Equation (1) in order to obtain the targeted Cr : V, i.e. (1-x) : x with *x*

ranging from 0.1 to 0.95. This reaction yields $(Cr_{1-x}V_x)_yO_z$ compounds where y:z is different from the targeted 2:3 ratio.

$$2x\ NH_4VO_3 + 2(1-x)\ Cr(NO_3)_3,9H_2O + 5\ C_6H_8O_7 + 15\ (NH_4)_2CO_3 \rightarrow (Cr_{1-x}V_x)_yO_z \qquad (1)$$

The aqueous solution was then concentrated on a hot plate at 100 °C until gelation started. On the course of concentration, Ammonium carbonate $(NH_4)_2CO_3$ was added in several portions to keep pH of the solution around 8. Basic condition was necessary to deprotonate Citric acid so that their COO^- groups can fix both V and Cr cations in their polymer gel networks. Otherwise, these free metal cations would have precipitated separately. As evaporation proceeded, the blue-purple solution became a gel, followed by self-combustion reaction that reduced the gel into brownish-grey powder. Once the water evaporation was completed, a first annealing treatment under oxygen flow at 480 °C during 8 hours aimed to trigger a pyrolysis reaction to burn and eliminate all the residual organic elements after reaction (1). A second treatment was carried out under a reducing flow of 95% Ar/ 5% H_2 with a first step at 550 °C during 22 hours and a second step at 900 °C during 22 hours to ensure the reduction of the different Vanadium/Chromium oxide phases towards $(Cr_{1-x}V_x)_2O_3$.

Single-crystals were grown from the previously synthesized powders using the chemical vapor transport method. First, a vacuum-sealed silica tube containing 200 mg of $(Cr_{1-x}V_x)_2O_3$ powder and 40 mg of sulfur (transport agent) was annealed at 1065 °C. At this temperature, the gaseous sulfur reacts with the volatized powder producing crystals at the cold side of the tube. The temperature was then slowly reduced (-0.5 °C/h) down to 930 °C, followed by a rapid cooling (-300 °C/h) down to room temperature. The chemical composition of the powder samples and crystals in terms of Cr/V content ratio was estimated using the Energy-dispersive X-ray spectroscopy (EDX) using a voltage source of 10kV.

Synthesis of V-substituted $(Cr_{1-x}V_x)_2O_3$ thin films

$Cr_{1-x}V_x$ or $Cr_{1-x}V_xO_y$ thin films were deposited by magnetron co-sputtering of two metallic Chromium (Cr) and Vanadium (V) targets, supplied by two independent direct current (DC) power sources, in a commercial AC450 sputtering chamber from Alliance Concept (France). Details on the equipment can be found in previous published work (M. Querré et al.)[21]. In. order to obtain $Cr_{1-x}V_x$ or $Cr_{1-x}V_xO_y$ thin films with x within the [0.06 – 0.96] range, the supplying powers of both targets were varied in the 100 – 300 W for the V target, and in the 15 – 300 W range for the Cr target. Thin films were deposited on Si/SiO_2 substrates in confocal configuration and two different modes: (i) a non-reactive mode in pure Ar atmosphere at a pressure P = 25 µbar for $Cr_{1-x}V_x$ films or (ii) a reactive mode in Ar/O_2 atmosphere (O_2/Ar ratio of 0.5%) for $Cr_{1-x}V_xO_y$ thin films. The deposition chamber was pumped down to 8.10^{-7} mbar prior to each deposition. For both modes, a post-annealing was necessary to obtain crystallized thin films with the targeted oxygen stoichiometry. All deposited thin films were submitted to an annealing step in a reducing flow of Ar/H_2 5% gas in a furnace previously pumped down to 10^{-3} mbar. Three different annealing conditions were performed, for a 10 h duration: (i) 500°C using a Cr/Cr_2O_3 oxygen buffer, (ii) 500°C using a Fe/Fe_3O_4 oxygen buffer and (iii) 800°C without buffer. The buffers consist in pressed pellets of either 142 mg of Cr / 207 mg of Cr_2O_3, or 73 mg of Fe / 100 mg of Fe_3O_4. As described by Rupp et al.[22], the use of such buffers guarantees that the annealing atmosphere follows the oxygen partial pressure needed to obtain stoichiometric $(Cr_{1-x}V_x)_2O_3$ thin films when annealing temperature evolves. Besides, annealing at 800°C in Ar/H_2 (5%) results in an oxygen partial pressure $ppO_2 = 10^{-21}$ atm, which ensures an annealing process leading to stoichiometric material[23].

Physicochemical characterizations of crystals, thin films and powders

The morphology of the deposited $(Cr_{1-x}V_x)_2O_3$ films was investigated by Scanning Electron Microscopy (SEM). Top view and cross section images were taken using a JEOL JSM 7600F SEM equipped with a Schottky field emission gun.

The chemical compositions and the V/Cr atomic ratios of $(Cr_{1-x}V_x)_2O_3$ single-crystals, polycrystalline powders and thin films were measured by Energy Dispersive Spectrometry (EDS). A JEOL JSM 5800LV SEM equipped with an energy dispersive spectrometer SDD SAMx set at 10 kV was used to characterize all samples.

Structural characterization of powders and thin films

X-Ray Diffraction (XRD) patterns of $(Cr_{1-x}V_x)_2O_3$ powders and thin films were recorded in Bragg Brentano geometry using a Bruker D8 series II diffractometer equipped with a Cu anode (Cu – Kα1 pure radiation). Diffraction peaks were attributed thanks to JCPDF files of ICSD database (#75577 for Cr_2O_3 and #64785 for $(Cr_{0.05}V_{0.95})_2O_3$). Le Bail refinement of the XRD patterns were performed using JANA 2020 software to determine the lattice parameters[24].

Raman spectra were recorded using a Renishaw Raman spectrometer equipped with an Ar source generating a 514 nm wavelength excitation. The spectra were collected on $(Cr_{1-x}V_x)_2O_3$ powders in the form of pressed pellets or directly on $(Cr_{1-x}V_x)_2O_3$ thin films. A backscattering geometry was used, with linearly polarized laser incoming light and no polarization for outgoing Raman scattered light.

Diffuse reflectance measurements

Diffuse reflectance measurements of the $(Cr_{1-x}V_x)_2O_3$ powders were performed using a Perkin Elmer lambda 1050 fitted with a 150 nm InGaAs integration sphere (250 - 2500 nm range). The

absorbance α was approximated with the Kubelka-Munk function given by Equation (2), where R is the measured diffuse reflectance. The Tauc method[25] was used to estimate the optical band gap through Equation (3) where α is the absorbance, $h\nu$ is the photon energy, β is a coefficient equal to ½ (2) for indirect (direct) band gap and E_g is the band gap energy.

$$F(R) = \frac{(1-R)^2}{2R} \approx \alpha \quad (2)$$

$$(\alpha h\nu)^{\beta} = h\nu - Eg \quad (3)$$

The edge of lowest energy peak (intersection of the linear fit of the plot with the x-axis) was used to estimate the band gap energy according to the Tauc's method. Some supporting data are given in ‘’Supporting Information’’.

Resistivity measurements

The electrical resistance of the $(Cr_{1-x}V_x)_2O_3$ crystals and $(Cr_{1-x}V_x)_2O_3$ thin films annealed under different conditions was measured at room temperature with the four points method using a Keithley 236 high voltage source-measure unit. The resistivity was calculated from the resistance after considering the shape and size of the samples.

Preparation of memory cell devices

The memory cells were prepared with $(Cr_{1-x}V_x)_2O_3$ thin films exhibiting different band gap values representative of this series of compounds. Three chemical compositions $(Cr_{1-x}V_x)_2O_3$ with x = 0.30, 0.7 and 0.95 were selected as they exhibit band gap values over the whole studied range: 0.7, 0.35 and 0.15 eV respectively. **Figure 1** gives a schematic draft of the Metal/Insulator/Metal (MIM) TiN/$(Cr_{1-x}V_x)_2O_3$/Au structure, based on 50 nm thick thin films, used for electrical testing. The circular via (here 2 µm diameter) obtained by photolithography and etching of the silicon

nitride (SiN_x) insulating layer allows to define and vary the contact size between the bottom electrode and the active film.

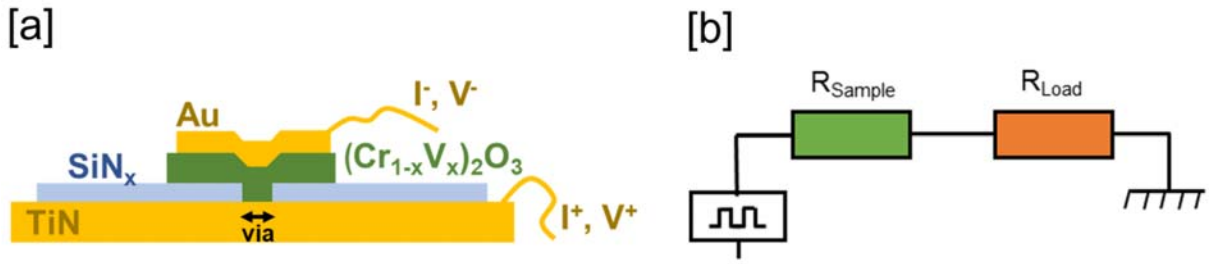

Figure 1: (a) Schematic section view of one memory cell in MIM structure. TiN electrodes sandwich the $(Cr_{1-x}V_x)_2O_3$ active film. A photolithographed etched hole in the SiN_x insulating film defines the small active region known as 'via' and the electric contact size. (b) Illustration of the electric circuit for operating one cell. A pulse generator and a resistance load (R_{load}) are connected in series with the cell (R_{sample}).

Resistive switching measurements

Resistive switching measurements were performed on memory cells based on MIM structure including $(Cr_{1-x}V_x)_2O_3$ (x = 0.3, 07, 0.95) thin films deposited either in reactive or non-reactive atmosphere and further annealed with iron buffer at 500 °C. Each device was connected in series to an external load resistance (noted R_{Load}) to ensure current limitation (see **Figure 1b**). R_{Load} ranges in the 10-80% of the device resistance. Electric voltage pulses (V_{tot}) were applied to these circuits (**Figure 1b**) using an Agilent 81150A voltage pulse generator. The High and Low Resistance States (HRS and LRS) were measured at low bias (10 mV) before and after the application of the electric pulses using a high-impedance Keithley 6430 source-measure unit. The voltage signal across the circuit and the load resistance was monitored with a DPO 3034 Tektronix oscilloscope. Devices prepared with thin films of same composition but deposited under reactive or non-reactive atmosphere exhibit very similar behaviors, including HRS and LRS with close values. Nevertheless, we noticed a better cycling endurance for MIM structures based on thin films prepared under reactive atmosphere, i.e. with oxygen during the deposition. For this reason, only those type of thin films will be considered in the last section dedicated to resistive switching.

RESULTS AND DISCUSSION:

Thin films deposition and annealing

Thin films of V-substituted Cr_2O_3 have been prepared through a two-step process, as detailed in the experimental section. First, pure metallic $Cr_{1-x}V_x$ films or $Cr_{1-x}V_xO_y$ with various V content (x varying in the 0.06 – 0.96 range) were deposited without intentional heating of the substrate. Secondly, the deposited films were *ex-situ* annealed in a highly reducing atmosphere, in order to crystallize oxide films with the accurate oxygen stoichiometry. It is worth noting that even in Ar/H_2 gas flow, the residual partial oxygen pressure was in the accurate range ($ppO_2 = 10^{-21}$ atm) to oxidize the metallic $Cr_{1-x}V_x$ thin films and obtain the targeted crystallized $(Cr_{1-x}V_x)_2O_3$ phase. As shown in previous works (Rupp *et al* [22]), thanks to the addition of Cr/Cr_2O_3 or Fe/Fe_3O_4 oxygen buffers, the oxygen partial pressure can be accurately controlled down to 10^{-37} atm and 10^{-23} atm respectively. Such oxygen pressure range allows obtaining the crystallization of thin films at lower annealing temperature, i.e. 500 °C instead of 800 °C.

A comprehensive study was performed for thin films deposited in non-reactive mode, (i.e. in pure Ar atmosphere and after annealing under controlled oxygen partial pressure) and, the main characterization results presented hereafter concern that type of films. But for comparison the results obtained on $(Cr_{1-x}V_x)_2O_3$ (x = 0.3, 07, 0.95) thin films deposited in reactive mode are also presented.

SEM images of as-deposited and annealed thin films with Cr/V atomic ratio of 30/70 are shown in **Figure 2**. As displayed, the as-deposited 35 nm thick thin film exhibits small grains in top view (**Figure 2 a**) and the typical columnar morphology of sputtered films in cross section (**Figure 2 b**). After annealing at 800°C under Ar/H_2 reducing flux, the film exhibits facetted grains at the surface (**Figure 2c**) and appears denser in cross section with a thickness increased to almost 50 nm and a grain size in the 50 ± 25 nm range (**Figure 2 d**). One can also note that the columnar structure of

the as-deposited film has disappeared. Thin film annealed at 500 °C with a Cr/Cr_2O_3 buffer is displayed in **Figure 2 e-f**. As seen in **Figure 2e**, the grain size appears intermediate between as-deposited and annealed at 800 °C. The cross-section view in **Figure 2f** confirms the granular morphology with smaller grain size than that annealed at 800°C, in the 30-50 nm range. Surface and cross-section SEM images of thin film after annealing at 500 °C with a Fe/Fe_3O_4 buffer are presented in **Figure 2 g-h** (non-reactive deposition) and **Figure 2 i-j** (film deposited in Ar/O_2). In both cases we observe a dense morphology with a grain size in the 30-50 nm range very similar to the film annealed with the Cr/Cr_2O_3 buffer. Comparing SEM images in **Figure 2 g-h and i-j,** the film deposited in reactive mode (last line) appears denser than the one deposited in non-reactive mode. Such morphology variation could account for the difference of electrical behavior observed later on (see last section).

As expected, the grain growth appears favored at higher temperatures and similarly impacted by both buffers when annealing at 500°C. However, the thin films annealed with a Fe/Fe_3O_4 buffer appear to be denser with well-defined grains and a better interface with the substrate than those annealed with the Cr/Cr_2O_3 buffer, especially in the case of thin film deposited in reactive mode (**Figure 2 i-j**). On this basis, the iron buffer was preferred to anneal the films deposited under pure Ar or in reactive conditions.

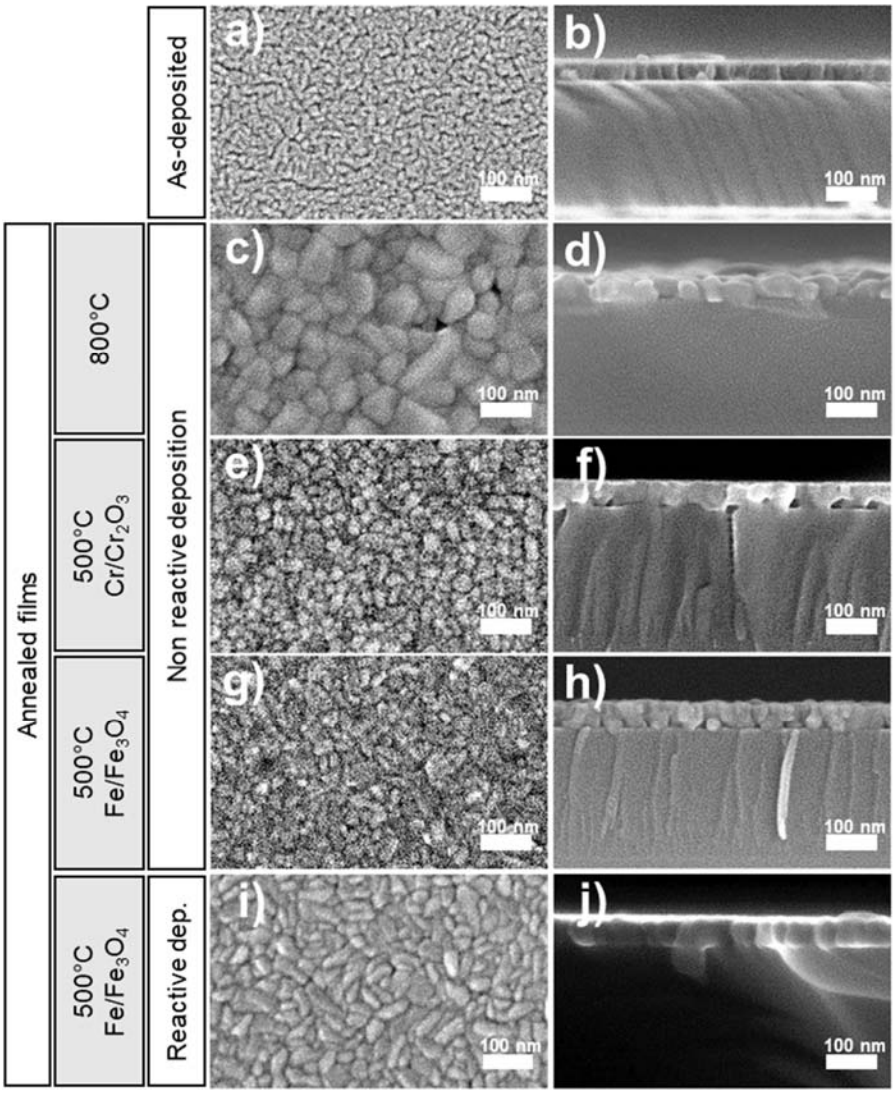

Figure 2. SEM images in top view (left column) and cross-section (right column) of $(Cr_{0,30}V_{0,70})_2O_3$ thin films when as deposited (a,b), annealed under a Ar/H_2 reducing flux at 800°C (c,d), at 500°C using a Cr/Cr_2O_3 oxygen buffer (e,f) at 500°C using a Fe/Fe_3O_4 oxygen buffer (g-j). Thin films were deposited by magnetron co-sputtering in non-reactive mode (a-h) and in reactive mode (i,j).

Structural Characterization of $(Cr_{1-x}V_x)_2O_3$ powders and thin films

To determine whether a continuous solid solution between V_2O_3 and Cr_2O_3 exists in thin films, in view of their integration into devices, a study of their crystalline structure was carried out. In the following, the discussion focusses on the results obtained with Fe/Fe_3O_4 buffer during the annealing step at 500 °C, since they are similar to those obtained with Cr/Cr_2O_3 buffer. The XRD patterns of $(Cr_{1-x}V_x)_2O_3$ thin films ($0.05 \leq x \leq 0.77$) deposited under pure Ar and annealed at 500 °C with Fe/Fe_3O_4 buffer are shown in **Figure 3.** XRD peak positions from JCPDS files of Cr_2O_3 phase (#75577) and $(Cr_{0.05}V_{0.95})_2O_3$ phase (#64785) from ICSD database are displayed (vertical bars) at the bottom and top of the figure (blue and brown lines respectively). XRD peaks between 32° and 33° are attributed to the Si (100) substrate – respectively double diffraction and (211) peaks. XRD diagrams of some selected films (x = 0.06; 0.37; 0.57; 0.76), annealed at 800 °C are displayed in supplementary data (**Figure S1).** In the case of thin films annealed at 500 °C with iron buffer (**Figure 3 a**), selected composition in the similar range are plotted (x = 0.08; 0.36; 0.57; 0.77). As seen, all patterns exhibit diffraction peaks that can be all attributed to the $R\bar{3}c$ crystalline structure described in Supporting Information (**Figure S2-a**). The (104) and (110) diffraction peaks (located at 33° and 36° respectively) are the most intense for all compositions, as expected from the theoretical intensities of the corresponding powder patterns. As shown, the deposited thin films generally display a (110) preferential orientation, without clear correlation between the peak intensity variations and the V content. Hence, this (110) preferential orientation is strongly marked for thin films deposited in reactive mode, as shown in **Figure 3** (c-d), and could explain the different electrical behaviors observed later on (see last section).

On the one hand, XRD peak positions for $(Cr_{1-x}V_x)_2O_3$ thin films with the lowest V content (x = 0.06 and 0.08) are close to the Cr_2O_3 diffraction peaks. On the other hand, diffraction peaks recorded for $(Cr_{1-x}V_x)_2O_3$ thin films with the highest V content (x = 0.76-0.77) are located close

to the ones of $(Cr_{0.05}V_{0.95})_2O_3$ reference. As displayed in the **Figure 3b** and **Figure 3d** focused on the (110) peak region, located close to 36°, a progressive shift of the peak position is observed over the whole range of chemical composition from the Cr_2O_3 (110) theoretical peak towards the $(Cr_{0.05}V_{0.95})_2O_3$ (110) peak, as the V content is increasing. A similar progressive shift of the (110) XRD peak is observed for both 500 °C and 800 °C annealing conditions (see **Figure S1**). **Figure 3c** shows XRD patterns, obtained for thin films deposited in reactive atmosphere (i.e. with oxygen) after annealing at 500 °C under Ar/H_2 gas flow during 10 h with the same Fe/Fe_3O_4 buffer, which are similar to the ones of thin films deposited in pure Ar after the same annealing. Hence, **Figure 3d** displays a zoom on the (110) peak region for the same x values. The same shift towards lower diffraction angles is observed as the V content is increasing in the films.

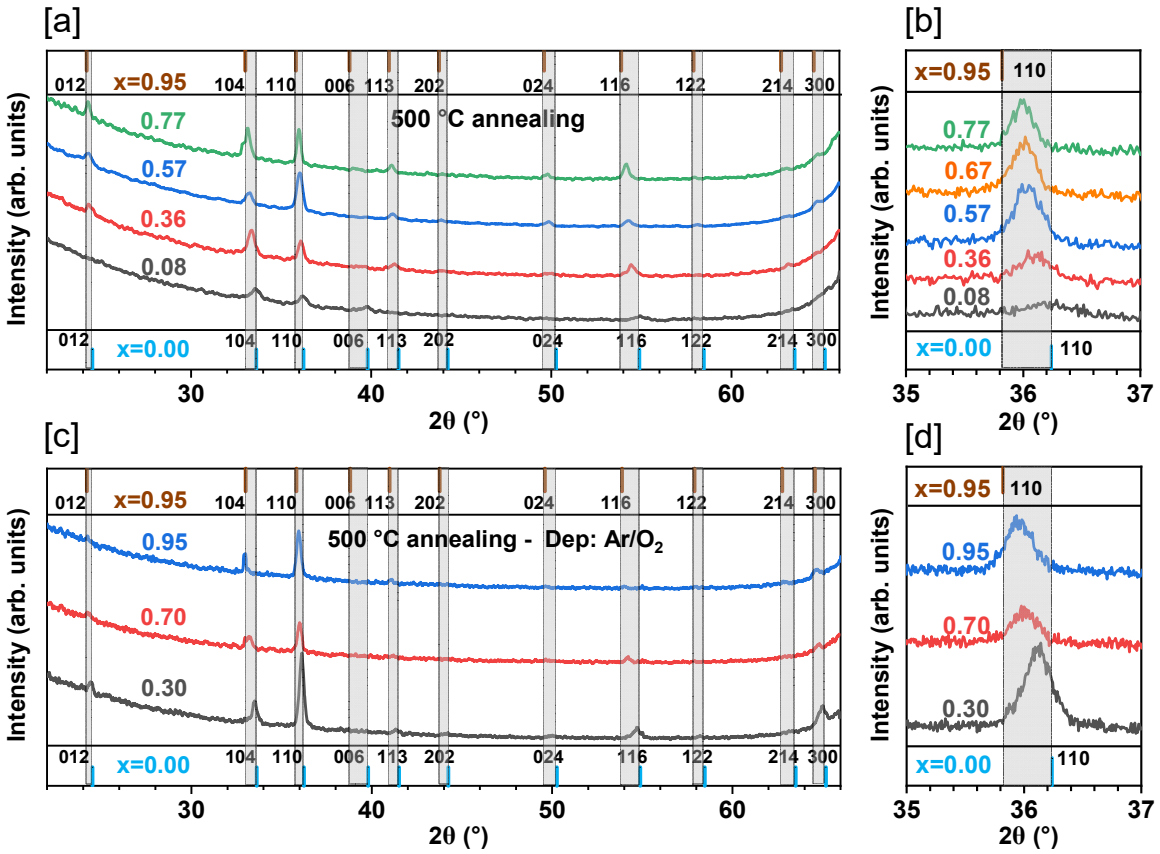

Figure 3 X-ray diffraction patterns of 50 nm thick $(Cr_{1-x}V_x)_2O_3$ films for V content in the range x = [0,08; 0,77]. Diffraction peaks of JCPDS Files #64785 (top) and #75577 (bottom) are displayed by vertical lines as references. Thin films deposited by non-reactive magnetron sputtering (a,b) and reactive mode (Ar/O_2) (c,d) after annealing at 500°C under a Ar/H_2 reducing flux with a Fe/Fe_3O_4 oxygen buffer. (a-c) Full-analyzed range and (b-d) Focus on the (110) diffraction peak.

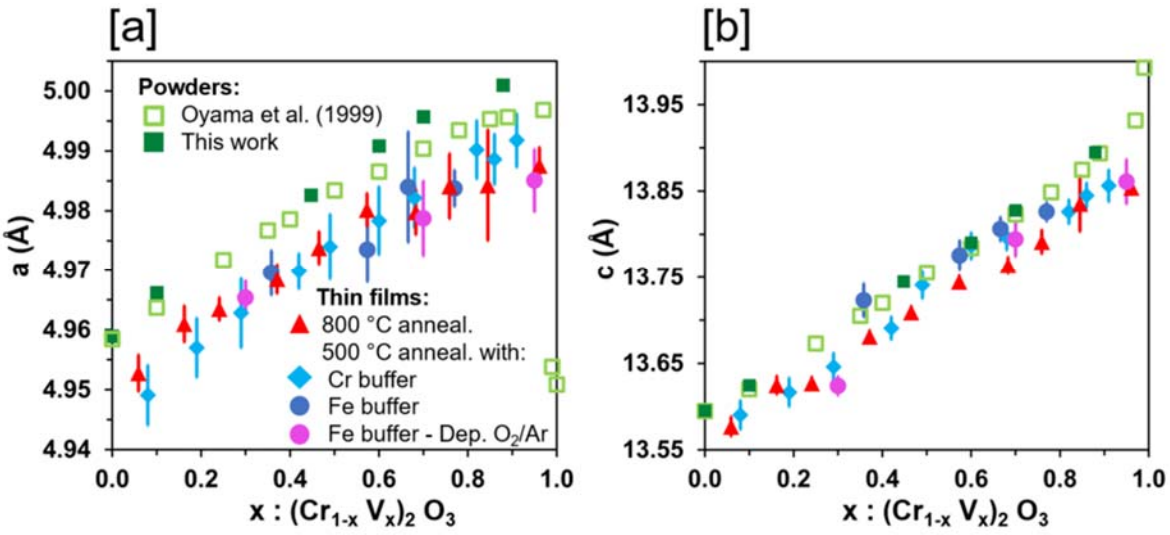

Figure 4 Evolution of the lattice parameter *a* (a) and *c* (b) for a 50 nm thick $(Cr_{1-x}V_x)_2O_3$ thin films compared to stoichiometric polycrystalline powders, obtained from the present work and Oyama et al.[26]. These thin films with V content between x = [0,06; 0,96] were annealed at 500 °C with Cr/Cr_2O_3 and Fe/Fe_3O_4 oxygen buffers, and 800°C without buffer. Thin films annealed at 500°C were deposited by reactive and non-reactive deposition magnetron sputtering.

To get more insights on the substitution, the evolution of the $(Cr_{1-x}V_x)_2O_3$ thin films lattice parameters versus the V content increase was investigated by Le Bail refinement of the XRD patterns. The evolutions of the two lattice parameters *a* and *c* versus the V content variation are displayed in **Figure 4 a-b**, respectively. As seen, these parameters increase monotonously when increasing the V content, with slightly higher values for powders than for the deposited and annealed films. Despite those differences, the *c/a* ratio also increases continuously when increasing the V content, but with closer values for thin films and powders (See in supporting information **Figure S3**). The variation of the *c* parameter is almost two times higher than *a* one, resulting in an expansion of the crystalline cell volume along the c-axis. Results are comparable for the three studied annealing conditions of thin films (see triangles, circles and diamonds). In addition, the evolution of both *a* and *c* parameters, after annealing at 500°C with Fe/Fe_3O_4 buffer, appears similar either in the case of thin films deposited in reactive atmosphere with oxygen or deposited in non-reactive atmosphere without oxygen (other experimental parameters unchanged, blue and

pink circles in **Figure 4.** The observed variation is significant of a unit cell expansion from 288 $Å^3$ for x = 0.06 up to 299 $Å^3$ for x = 0.96 in the case of thin films, and from 289 $Å^3$ for x = 0 up to 301 $Å^3$ for x = 0.88 in the case of powders (See Supplementary Information figure S3).

The linear dependence of the lattice parameters versus the V content variation observed for $(Cr_{1-x}V_x)_2O_3$[26] thin films and powders is consistent with Vegard's law in solid solutions[27]. Besides, a uniform and complete V-Cr substitution in Cr_2O_3 is possible because V and Cr atoms have very close atomic radius, electronegativity and valence states. Similarly to published results for powders[22], $(Cr_{1-x}V_x)_2O_3$ thin films annealed at 800 °C or 500°C (either with Cr/Cr_2O_3 or Fe/Fe_3O_4 buffer) lead to a substitutional solid solution on the entire range of V/Cr atomic ratio.

In the case of powders, we also plot the results of this work (bold squares) with published results of Oyama[26] (open squares in all graphs of **Figure 4**). The *a* and *c* lattice parameters are in good agreement with previous published results, especially for lower V content (x < 0.6) where cell parameters values match remarkably. Nevertheless for thin films, *a* and *c* parameters are always lower than for polycrystalline powders (Δa = -0.01 Å and Δc = -0.03 Å, respectively). Hence, one observes a similar difference with results by Oyama et al.[26] for x < 0.6. The corresponding reduction of unit cell volume in thin films is approximately ΔV = -2 $Å^3$ compared to powders. Such variation can be generated either by internal stress within the deposited film or by a slight oxygen non-stoichiometry. The later hypothesis will be eliminated by the resistivity measurements as detailed in the last section. Thermal residual stress generated during the annealing step, due to the different thermal expansion coefficients of thin film and substrate, is then the most likely explanation for the observed difference of lattice parameters.

Raman study of $(Cr_{1-x}V_x)_2O_3$ powders and thin films

The structural properties were further investigated for both V-substituted Cr_2O_3 thin films and powders by Raman spectroscopy. Based on symmetry arrangements[28], V-substituted Cr_2O_3 compounds should exhibit five E_g and two A_{1g} Raman modes. Nevertheless, only A_{1g} modes (**Figure 5 a**) have enough intensity to be clearly detected with a 514 nm wavelength excitation. In addition, the intense peak of Si/SiO_2 substrate (in grey) hides a part of the Raman spectra. In **Figure 5 b-d**, the blue vertical lines at the bottom stand for the Raman modes given in literature for Cr_2O_3 powder[29]. **Figure 5b** displays Raman spectra of two thin films (composition x = 0.96 and x = 0.) annealed at 800 °C show only $A_{1g}(1)$ or $A_{1g}(2)$ modes for the highest and lowest V contents, respectively. As described in **Figure 5 a**, $A_{1g}(1)$ mode is associated to the M-M dimer vibration (M: V, Cr) along c axis, i.e. the shortest M-M distance and $A_{1g}(2)$ mode is the breathing of the oxygen atoms in the basal plane[30]. Hence, at low V content, only the vibration mode involving oxygen can be detected, whereas at higher V content, the V-Cr elongation mode becomes intense enough to be detected. The evolution of the two Raman modes in the different films when the V content increases (x in the 0.06 - 0.96 range) is shown in **Figure 5c** and **Figure 5d**, for $A_{1g}(1)$ and $A_{1g}(2)$ modes respectively. The $A_{1g}(1)$ mode emerges and becomes visible above x=0.16 and the intense $A_{1g}(2)$ mode disappears above x=0.57. As earlier said, the intensity of the $A_{1g}(1)$ mode increases with the increase of V content, meanwhile the $A_{1g}(2)$ mode intensity decreases conversely, as also observed on pressed polycrystalline powders (See Figure S5 in supplementary data) in good agreement with published data[27].

In **Figure 5 e,** the evolutions of both A_{1g} modes positions are plotted for stoichiometric powders (pressed pellets, see **Figure S4** in Supporting Information) and thin films annealed at 800°C and 500°C with Cr/Cr_2O_3 and Fe/Fe_3O_4 buffers. In all cases, the two modes shift continuously to lower

frequencies as the Vanadium content is increased and finally drop for the higher V content (above x = 0.96), when the material is close to V_2O_3 oxide.

Tatsuyama *et al.*[26] concluded that the phonon modes evolution in V-substituted Cr_2O_3 while increasing the V content was accompanied by an increase of the lattice parameters going along with increase of both M-M and O-O atomic distances which are promoted by the Cr substitution by V atoms. The evolution of Raman modes in V-substituted Cr_2O_3 powders and thin films thus correspond to a softening of the $A_{1g}(1)$ and $A_{1g}(2)$ modes initially identified in Cr_2O_3. In our study, the M-M distance associated to the $A_{1g}(1)$ mode increases continuously from 3.43 Å (x=0.00) up to 3.45 Å (x=0.85). In addition, **Figure 5e** shows that the frequency of the two A_{1g} modes decreases linearly with V content increase up to x=0.98 and further decreases to reach the V_2O_3 frequency. Such results well agree with the expansion of the unit cell volume observed in previous section when x varies from 0.00 up to 0.97. The good agreement in the A_{1g} modes evolution, observed for both powders and thin films, highlights that Raman spectroscopy could be a good tool to estimate accurately the V content and check the chemical homogeneity of thin films at the micrometer scale.

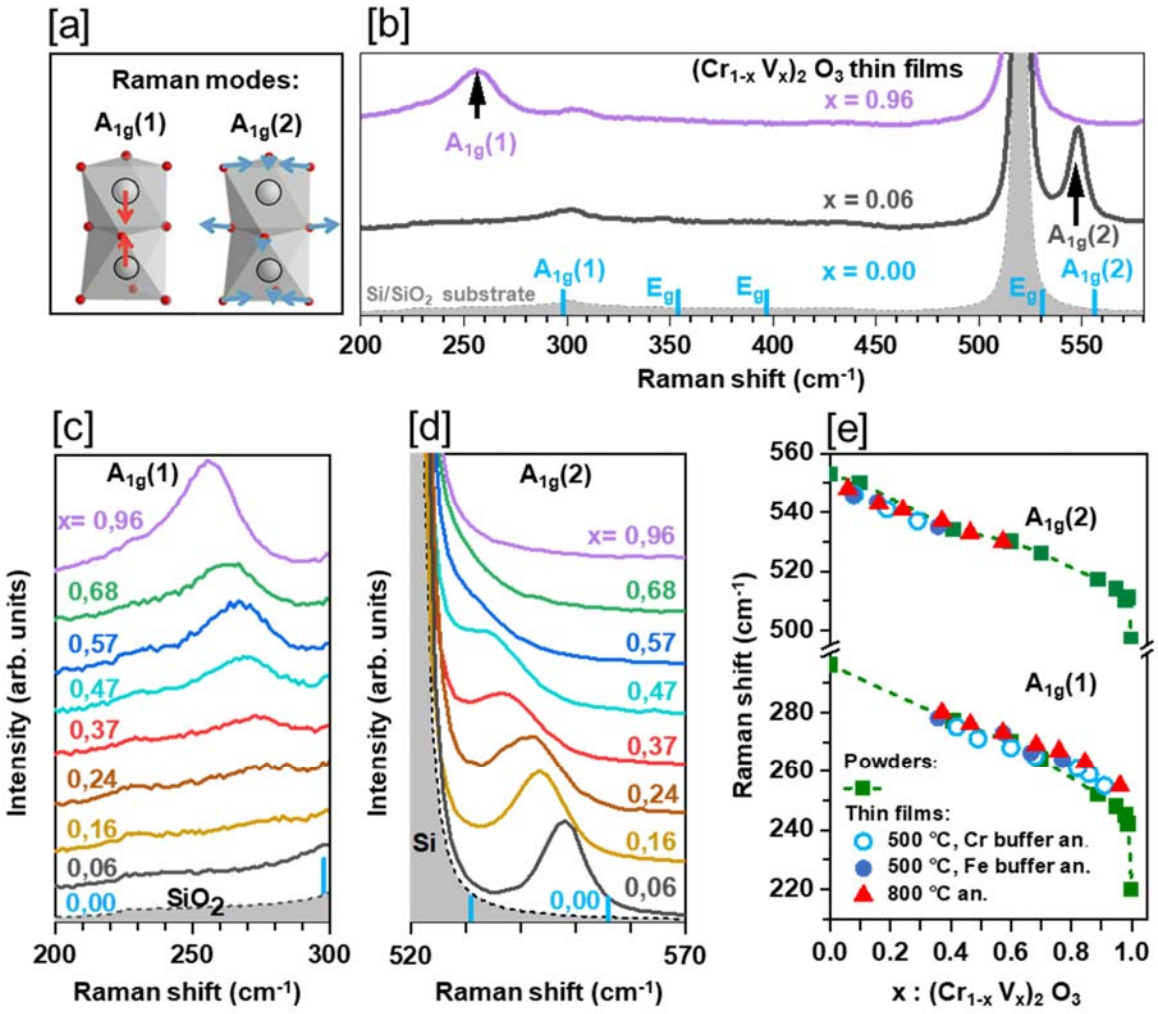

Figure 5 (a) Atomic displacements corresponding to Raman modes $A_{1g}(1)$ and $A_{1g}(2)$ of $(Cr_{1-x}V_x)_2O_3$ (b) Raman spectra of 50 nm thick $(Cr_{1-x}V_x)_2O_3$ polycristalline thin films deposited on Si/SiO_2 substrates and annealed at 800 °C. Evolution of the (c) $A_{1g}(1)$ and (d) $A_{1g}(2)$ modes in thin films with V content x = [0,06; 0,96], annealed at 800 °C. (e) Evolution of the $A_{1g}(1)$ and $A_{1g}(2)$ modes in thin films annealed at 500 °C with Cr/Cr_2O_3 and Fe/Fe_3O_4 oxygen buffer and 800°C compared to stoichiometric polycrystalline powders. The blue lines at the bottom of panels b-d gives the Raman modes of a Cr_2O_3 powder, obtained from the study of Shim et al.[29].

Electrical characterization of V-substituted Cr_2O_3 thin films.

The impact of the vanadium content on the resistivity and optical band gap of the $(Cr_{1-x}V_x)_2O_3$ compounds was investigated. Thin films prepared under Ar atmosphere and annealed in the previous detailed conditions at 800 °C and 500 °C were characterized. As reference, single crystals with various contents of V (x ranging from 0.24 to 0.96) were also analyzed (see experimental

section for synthesis details. **Figure 6a** presents the evolution of electrical resistivity measured using the 4-points method at room temperature versus the V content in $(Cr_{1-x}V_x)_2O_3$ thin films and single crystals. For the entire studied range, the resistivity decreases sharply when the V content increases, from $\rho = 5.10^4$ Ω.cm for $(Cr_{0.76}V_{0.24})_2O_3$ down to $\rho = 2$ Ω.cm for $(Cr_{0.04}V_{0.96})_2O_3$, i.e. a variation of four orders of magnitude. The same trend is observed for all thin films and all annealing conditions (temperature and buffer). Moreover, the obtained resistivity values for thin films are in good accordance with those of single-crystals. Such results stands as a good guarantee of the films quality in terms of crystallinity.

Optical characterization of V-substituted Cr_2O_3 thin films.

The Tauc plots extracted from diffuse reflectance spectra of $(Cr_{1-x}V_x)_2O_3$ powders are given in Supporting Information (**Figure S5**). They were used to determine the optical band gap variation versus the V content. According to the Tauc's method explained in the experimental section, the edge of lowest energy peak was used to estimate the band gap energy. In the case of Cr_2O_3 (x = 0), variations of spectral weight observed between 2 and 3 eV correspond to intra-atomic excitations and thus are not relevant for the band gap estimation.

The evolution of extracted band gap values as a function of V content x is plotted in **Figure 6b**. Note that purple symbols are values from literature[31,32] and appear in quite good agreement with our experimental results. As seen, a sharp drop of the band gap occurs as soon as some V is substituted. The band gap decreases from ≈ 3eV for pure Cr_2O_3 to 0.75 for $(Cr_{0.9}V_{0.1})_2O_3$ (x = 0.1). For higher V content up to x = 0.6, the band gap is almost stable and then slowly decreases with further V content increase down to zero, i.e. the metallic state in V_2O_3. The reduction of the resistivity within the solid solution seen in **Figure 6a** is in accordance with the evolution of the band gap.

To better understand the origin of this band gap evolution, **Figure 6c** shows a schematic illustration of the electronic structures of V_2O_3, $(Cr_{0.50}V_{0.50})_2O_3$ and Cr_2O_3 adapted from DFT+U calculations of Le *et al.*[33]. In this figure, the electronic bands close to the Fermi level, which participate in the electronic conduction, are labeled in bold. In Cr_2O_3, a large gap around 3 eV occurs between the t_{2g} spin up band of chromium 3d character completely filled by 3 electrons (Cr^{3+} ➔ $3d^3$) and the empty e_g band. When V substitutes Cr in Cr_2O_3, band structure calculations indicate that the vanadium 3d t_{2g} levels are located above the occupied t_{2g} levels of Cr (**Figure 6c**).

Because of the trigonal distortion of the octahedron VO_6 in the corundum structure, vanadium t_{2g} levels are splitted into e_g^{π} and a_{1g} levels. Since the valence of vanadium atoms is V^{3+} / $3d^2$ in $(Cr_{1-x}V_x)_2O_3$, the two Vanadium 3d electrons populate only the spin *up* e_g^{π} levels ($e_g^{\pi}{}_{\uparrow}$). The vanadium e_g^{π} band is indeed half-filled (= populated by 2 over 4 possible electrons), and split in $e_g^{\pi}{}_{\uparrow}$ and $e_g^{\pi}{}_{\downarrow}$ levels due to electron-electron repulsion. In this context, the gap for all the solid solution $(Cr_{1-x}V_x)_2O_3$ occurs exclusively between bands of vanadium character, specifically between the fully occupied spin up $e_g^{\pi}{}_{\uparrow}$ band and the unoccupied $a_{1g\uparrow}$ band. This scenario explains the sharp drop of the gap between Cr_2O_3 (3 eV) and lightly-substituted $(Cr_{1-x}V_x)_2O_3$ (0.75 eV). At low V content x, the vanadium e_g^{π} and a_{1g} bands mostly behave as narrow impurity levels. As V content x increases, these levels widen as bands, therefore reducing progressively the e_g^{π} (spin up) to a_{1g} band gap of $(Cr_{1-x}V_x)_2O_3$, from 0.75 eV at low x to ≈ 0.2 eV at x = 0.81. This scenario also explains the continuous increase of spectral weight in the 1-2 eV energy range shown in (**S6-**supplementary data). The excitation intensity of V $e_g^{\pi}{}_{\uparrow} \rightarrow$ V $a_{1g\uparrow}$ indeed increases proportionally to V content.

Finally, the complete solid solution $(Cr_{1-x}V_x)_2O_3$ was obtained in thin films and these correlated insulating materials show a band gap decreasing when increasing the vanadium content. The reduction of resistivity observed when the V content increases is in good agreement with this

evolution of the optical band gap within the solid solution (**Figure 6 a-b**). Moreover both trends are consistent with the description of the electronic structure of the $(Cr_{1-x}V_x)_2O_3$ correlated insulators based on DFT+U modelling.

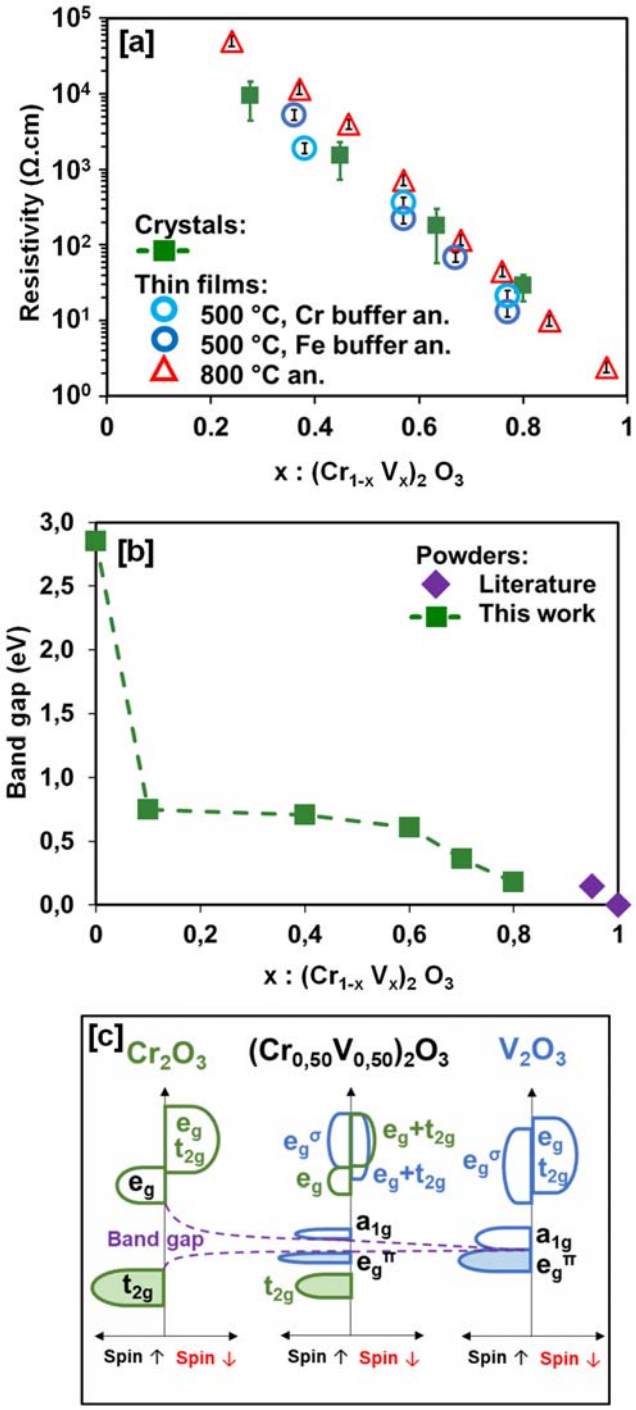

Figure 6 (a) Evolution of electric resistivity of 50 nm $(Cr_{1-x}V_x)_2O_3$ thin films for the different annealing conditions and comparison with resistivity of stoichiometric single crystals. (b) Evolution of the optical band gap of $(Cr_{1-x}V_x)_2O_3$ with the V content. Values for high V content (x= 0.95 and 1) compounds are extracted from literature[31,32] (c) Schematic evolution of the electronic structure of $(Cr_{1-x}V_x)_2O_3$ upon V substitution considering the evolution of the band gap and DFT+U simulations of H.-L. Le et al. [33].

Resistive switching properties of memory cells made of V-substituted Cr_2O_3 thin films

The influence of the band gap on the characteristics of the resistive switching operation was investigated on memory cells prepared with $(Cr_{1-x}V_x)_2O_3$ thin films with various amount of vanadium (x= 0.05, 0.7and 0.95) and band gaps (0.7, 0.35 and 0.15 eV respectively). **Figure 7a** shows the evolution of the pristine resistance of the measured cells (green dots) as a function of the composition x of V-substituted thin films. The measured pristine resistances (65 MΩ for x = 0.3, 30 kΩ for x = 0.7 and 5 kΩ for x = 0.95) show a good agreement with the expected values (17 MΩ for x = 0.3, 22 kΩ for x = 0.7 and 1.3 kΩ for x = 0.95) calculated from the film resistivity for a 2 µm diameter contact size (see Figure 7a).

Figure 7a also displays the Low Resistance State R_{ON} (black dots) observed after a first SET and the High Resistance State R_{OFF} (red dots) measured after the first RESET. For each device, a clear resistive switching cycle is observed, and R_{OFF} comes back close to the pristine value. This behavior has been previously observed in narrow gap Mott insulators and attributed to the quasi-complete dissolution of the filament[12,15]. **Figure 7b** shows the average values of R_{ON} and R_{OFF} measured on 10 devices made with thin films of each composition x= 0.05, 0.7 and 0.95. The range of measured values shown by the error bars indicates the small variability among the 10 devices. The R_{OFF} is close to the pristine value and increases drastically when decreasing the vanadium content. On the other hand, the R_{ON} shows a smaller variation (**Figure 7b**) which results in the resistive memory window enlargement (R_{OFF}/R_{ON}) when decreasing the vanadium content (**Figure 7c**). The largest memory window is obtained for the composition x = 0.7 with a R_{OFF}/R_{ON} of the order of 10^4.

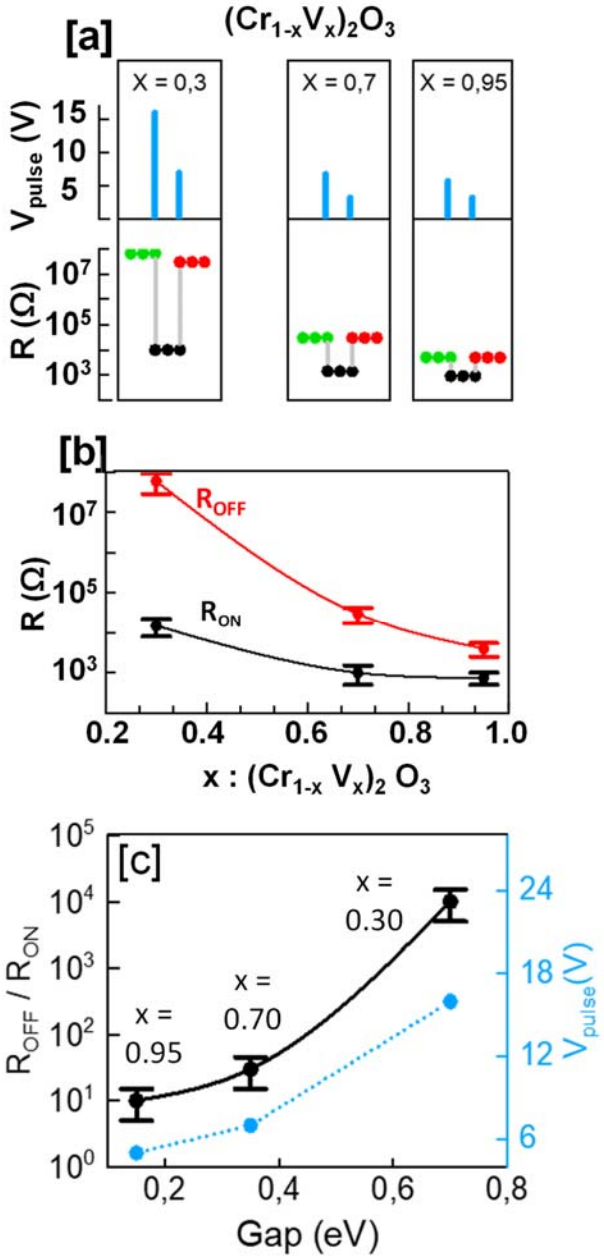

Figure 7. (a) First RS cycle on three cells based on thin films with the following chemical composition: $(Cr_{0.05}V_{0.95})_2O_3$, $(Cr_{0.30}V_{0.70})_2O_3$ and $(Cr_{0.70}V_{0.30})_2O_3$. Green dots represent the pristine state, black dots represent the low resistive state R_{ON} after the first SET and red dots represent the high resistive state R_{OFF} after the first RESET. Blue bars represent the voltage of the electric pulses used for the SET (left bar) and RESET (right bar). (b) Evolution of the first R_{OFF} and R_{ON} states versus the V content in the active film. The error bars given for each composition represent the variation of measured values for ten different cells on a same device. (c) Evolution of the RS amplitude (R_{OFF}/R_{ON}) and the voltage applied for the SET (V_{pulse}) of the same cells versus the gap value of the corresponding active layers. For these experiments and for the three tested chemical compositions (x = 0.3, 0.7 and 0.95) we used R_{Load} = 1 MΩ, 10 kΩ and 3.3 kΩ for SET respectively, and R_{Load} = 0 for RESET, and the films were deposited under reactive atmosphere.

These results emphasize a clear dependence of R_{ON} and R_{OFF} and of the ratio R_{OFF}/R_{ON} with the composition x. **Figure 7**c shows the evolution of R_{OFF}/R_{ON} measured for the three types of devices previously described versus the gap of the corresponding films. This figure confirms that the memory window is increased with increasing the band gap within the series of compounds. On the other hand, the applied voltage pulses necessary to induce the first SET also increases with the band gap (see **Figure 7a** and ***Figure 7***c).

This trend is not surprising since the threshold voltage of the volatile resistive transition in Mott insulators was demonstrated to vary with the gap[10], and non-volatile transitions have systematically been observed to appear for voltages 3-4 times higher than this threshold voltage. These results are also in agreement with the enhancement of the resistive switching amplitude R_{OFF}/R_{ON} observed previously on GaV_4S_8 based devices (0.3 eV) with respect to $(Cr_{0.05}V_{0.95})_2O_3$ (0.15 eV) based devices with an equivalent via size[15]. These results support therefore that the band gap is a key parameter to tune the memory window *i.e.* the R_{OFF}/R_{ON} ratio of these correlated insulating material.

To investigate further the effect of a larger gap on the resistive switching, devices based on a well-crystallized 50 nm thick $(Cr_{0.3}V_{0.7})_2O_3$ thin film were prepared and dedicated to perform endurance tests. **Figure 8a** shows that devices with this composition exhibit 1000 RS cycles using short electric pulses of V_{tot} = 5.4 V (3.8V on the cell) / 100 ns for the SET and 3.3 V / 800 ns for the RESET. The cumulative distribution function (CDF) curve, used to compare the distributions of resistance values for different resistive states, shows in **Figure 8b** an average R_{OFF}/R_{ON} ratio close to 16.

The device-to-device (D2D) variability was investigated using 10 devices of the same composition x = 0.7, fabricated on several samples. **Figure 8c** and **Figure 8d** show for these devices the variation of the values of the switching voltages (V_{SET}, V_{RESET}) and resistance states (R_{OFF}, R_{ON}), respectively. On the one hand, the switching voltage average is around 6 V (4.2V on the cell) and 3.9 V for the SET and RESET, respectively. It can be noted that V_{SET}, ranging from 4.5 to 7.4 V (3.1 to 5.2V on the cell), displays higher D2D variability than V_{RESET}, in the 3.2- 3.8 V range. On the other hand, the average values of resistance are around 10 kΩ and 1 kΩ for R_{OFF} and R_{ON}, respectively, demonstrating low variability. In addition, the resistance of two programmed devices was measured during 12 days at room temperature in order to evaluate the data retention of both states R_{OFF} and R_{ON}.

The results shown in **Figure 8e** indicate that the high and low resistive states show no significant variation after 12 days, and that the retention of R_{OFF} and R_{ON} states can be extrapolated up to 10 years. All these performances are comparable with the one observed on $(Cr_{0.05}V_{0.95})_2O_3$ thin films with lower band gap [9]. It suggests that increasing the band gap within the series $(Cr_{1-x}V_x)_2O_3$ may be a suitable way to increase the memory window without lowering the memory performances. In order to get more insights in the resistive switching mechanism and performances of the solid solution, further investigations of materials with higher V content are under progress.

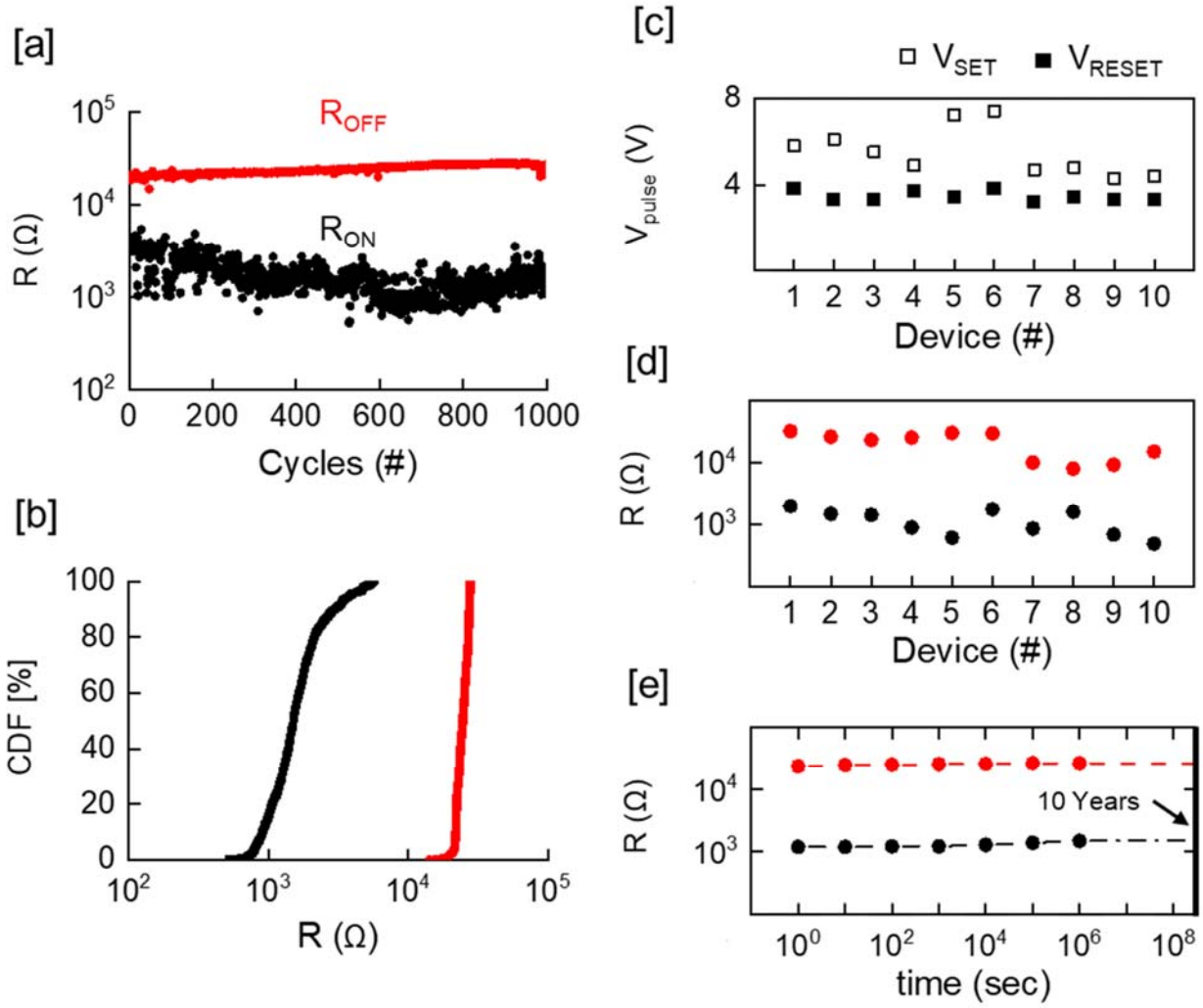

Figure 8 (a) Cycling endurance obtained on a device prepared with a 2 µm via and 50 nm thick $(Cr_{0.3}V_{0.7})_2O_3$ thin film and showing 1000 resistive switching cycles. (b) Cumulative distribution function of the high (R_{OFF}) and low (R_{ON}) resistive states represented in panel (a). Device to device (D2D) variability for SET and RESET applied pulses (c), and R_{ON} / R_{OFF} Resistances (d) measured for 10 devices. (e) Data retention at room temperature extrapolated to 10 years for HRS and LRS. For these experiments we used R_{Load} = 10 kΩ for SET and R_{Load} = 0 Ω for RESET, and the films were deposited under reactive atmosphere.

CONCLUSION:

V-substituted Cr_2O_3 compounds have been synthesized in single crystal, polycrystalline powders and thin films. Several compositions were deposited in thin films by magnetron co-sputtering of two vanadium and chromium metallic targets. Their structural, optical and electrical properties have been widely investigated versus the V content. For the entire range of chemical composition $(Cr_{1-x}V_x)_2O_3$ $(0<x<1)$, those compounds crystallize in the same $R\bar{3}c$ symmetry with a monotonous cell parameters evolution. XRD and Raman spectroscopy analyses demonstrated that annealed $(Cr_{1-x}V_x)_2O_3$ thin films stand as a solid solution over the whole range of x values, as already known for single crystals and powders. Physico-chemical, structural and optical properties of the annealed thin films are in close agreement with those of polycrystalline powders. No significant difference was observed between thin films deposited in non-reactive or reactive magnetron sputtering, i.e. in pure Ar or Ar/O_2 gas mixture. As the V content increases, the insulator character of $(Cr_{1-x}V_x)_2O_3$ compounds is worsening with a resistivity variation from 5.10^4 Ω.cm for $(Cr_{0.76}V_{0.24})_2O_3$ down to 2 Ω.cm for $(Cr_{0.04}V_{0.96})_2O_3$. In thin films, the optical band gap variation is similar to reported values for bulk materials, i.e. this value evolves from 3 eV for Cr_2O_3 to 0 eV and a metallic state for V_2O_3 as the V content increases. MIM devices based on $(Cr_{1-x}V_x)_2O_3$ deposited films show a non-volatile resistive switching with an enhanced amplitude R_{OFF}/R_{ON} ratio for lower V contents. The obtained large memory window appears to be associated with a high gap value. The demonstrated potential to obtain two highly differentiated resistive states (R_{OFF} and R_{ON}) is favorable for high reliability of data storage and non-volatile memory applications. A first study of non-volatile resistive switching has been performed on devices based on a 50 nm thick $(Cr_{0.7}V_{0.3})_2O_3$ film, characterized by a gap value of 0.7 eV. The performances appear very interesting for further memory applications with the following characteristics: a 1000 endurance cycles, a low device-to-device

variability and a data retention reasonably extrapolated to 10 years. Lastly, this work demonstrates the existence of a substitutional solid solution with tunable gap in thin films, which could be of great interest for enhancing data storage characteristics of correlated insulators. Large gap correlated insulators stand thus as interesting materials for non-volatile memory applications with a large memory window.

Supporting Information (pdf file)

- X-ray diffraction patterns of 50 nm thick $(Cr_{1-x}V_x)_2O_3$ films with V contents in the range x = [0,06; 0,96] and deposited by non-reactive magnetron sputtering after annealing under a Ar/H_2 reducing flux at 800°C. (a) Full-analyzed range and (b) Focus on the (110) diffraction peak;

- Illustration of the hexagonal crystalline structure of the Cr_2O_3 and the V-substituted Cr_2O_3 (space group $R\bar{3}c$) and the phase diagram of $(Cr_{1-x}V_x)_2O_3$ adapted from literature[34, 35].

- Evolution of the c/a ratio and the unit cell volume V for a 50 nm thick $Cr_{1-x}V_x)_2O_3$ thin compared to stoichiometric polycrystalline powders from this work and literature[26].

- Raman spectra of $(Cr_{1-x}V_x)_2O_3$ powder samples with V content 'x' in the 0.00 to 0.95 range with highlighted indication of corresponding Raman modes.

- Tauc plots obtained by diffuse reflectance measurements in the 0.5-4.0 eV range for stoichiometric $(Cr_{1-x}V_x)_2O_3$ powders with V content x in the 0-0.81 range, associated to a short discussion.

- Comparison between our work on the Cr_2O_3-V_2O_3 solid solution and the Cr_2O_3-Fe_2O_3 adapted from Ref. [36].

Acknowledgments

M. Rodriguez-Fano thanks the University of Nantes for funding his PhD. M. Haydoura is grateful to the Nano2022IPCEI project for funding his Postdoctoral fellowship. J.-Y. Mevellec is

acknowledged for Raman measurements. Thanks are due to the Region Pays de La Loire for funding the project Mott-IA.

REFERENCES

(1) Lee, G. H.; Hwang, S.; Yu, J.; Kim, H. Architecture and Process Integration Overview of 3D NAND Flash Technologies, Appl. Sci., 2021, 11, 6703-6720.
(2) Cai, Y.; Ghose, S.; Haratsch, E. F.; Luo, Y.; Mutlu, O. Error Characterization, Mitigation, and Recovery in Flash-Memory-Based Solid-State Drives, Proceedings IEEE, 2017, 105, 1666-1704.
(3) Chen A. A review of emerging non-volatile memory (NVM) technologies and applications, Solid-State Elec., 2016, 125, 25-38.
(4) Banerjee W.; Challenges and Applications of Emerging Nonvolatile Memory Devices, Electronics, 2020, 9, 1029-1042.
(5) Liu, B.; Wei, T.; Hu, J.; Li, W.; Ling, Y.; Liu, Q.; Cheng, M.; Song, Z. Universal Memory Based on Phase-Change Materials: From Phase-Change Random Access Memory to Optoelectronic Hybrid Storage, Chinese Phys. B, 2021, 30, 058504-(1-22).
(6) Hwang, C. S.; Mikolajick, T. Ferroelectric Memories, Eds. Magyari-Köpe, B., Nishi, Y., in Woodhead Publishing Series in Electronic and Optical Materials, Advances in Non-Volatile Memory and Storage Technology (Second Edition), Woodhead Publishing, 2019, 393–441.
(7) Prenat, G.; Jabeur, K.; Di Pendina, G.; Boulle, O.; Gaudin, G. Beyond STT-MRAM, Spin Orbit Torque RAM SOT-MRAM for High Speed and High Reliability Applications. In Spintronics-based Computing; Zhao, W., Prenat, G., Eds.; Springer International Publishing: Cham, 2015; 145-157.
(8) Sbiaa, R.; Piramanayagam, S. N. Recent Developments in Spin Transfer Torque MRAM, Phys. Stat. Sol. RRL, 2017, 11, 17001-(63-70).
(9) Wang, C.; Wu, H.; Gao, B.; Zhang, T.; Yang, Y.; Qian, H. Conduction Mechanisms, Dynamics and Stability in ReRAMs, Microelec. Eng., 2018, 187, 121-133.
(10) Imada, M.; Fujimori, A.; Tokura, Y. Metal-Insulator Transitions, Rev. Mod. Phys., 1998, 70, 1039-1263.
(11) Janod, E.; Tranchant, J.; Corraze, B.; Querré, M.; Stoliar, P.; Rozenberg, M.; Cren, T.; Roditchev, D.; Phuoc, V. T.; Besland, M.-P.; Cario, L. Resistive Switching in Mott Insulators and Correlated Systems, Adv. Funct. Mater., 2015, 25, 6287-6305.
(12) Guiot, V.; Cario, L.; Janod, E.; Corraze, B.; Ta Phuoc, V.; Rozenberg, M.; Stoliar, P.; Cren, T.; Roditchev, D. Avalanche Breakdown in $GaTa_4Se_{8-x}Te_x$ Narrow-Gap Mott Insulators, Nat. Commun., 2013, 4, 1722-1727.
(13) Diener P. ; Janod E. ; Corraze B. ; Querré M. ; Adda C. ; Guilloux-Viry M. ; Cordier S. ; Camjayi A. ; Rozenberg M. ; Besland M.-P.; Cario L. How DC-Electric Field Drives Mott Insulators Out of Equilibrium, Phys. Rev. Lett., 2018, 121, 016601-(1-6).
(14) Tranchant, J.; Janod, E.; Corraze, B.; Stoliar, P.; Rozenberg, M.; Besland, M.-P.; Cario, L. Control of resistive switching in AM_4Q_8 narrow gap Mott insulators: a first step towards neuromorphic applications, Phys. Stat. Sol. A, 2015, 212,239-244.
(15) Vaju, C.; Cario, L.; Corraze, B.; Janod, E.; Dubost, V.; Cren, T.; Roditchev, D.; Braithwaite, D.; Chauvet, O. Electric-Pulse-Driven Electronic Phase Separation, Insulator-Metal Transition, and Possible Superconductivity in a Mott Insulator, Adv. Mater., 2008, 20, 2760-2765.

(16) Souchier, E.; Cario, L.; Corraze, B.; Moreau, P.; Mazoyer, P.; Estournès, C.; Retoux, R.; Janod, E.; Besland, M.-P. ; First Evidence of Resistive Switching in Polycrystalline GaV_4S_8 Thin Layers, Phys. Stat. Sol. RRL, 2011, 5, 53-55.
(17) Tranchant, J.; Querre, M.; Janod, E.; Besland, M.-P.; Corraze, B.; Cario, L. Mott Memory Devices Based on the Mott Insulator $(V_{1-x}Cr_x)_2O_3$, IEEE International Memory Workshop (IMW); Proceeding IEEE: Kyoto, 2018, 1-4.
(18) Cario, L.; Tranchant, J.; Corraze, B.; Janod, E. Correlated Transition Metal Oxides and Chalcogenides for Mott Memories and Neuromorphic Applications. In Metal Oxides for Non-volatile Memory, Dimitrakis, P., Valov, I., Tappertzhofen, S., Eds.; Metal Oxides; Elsevier, 2022; 307–360.
(19) Lee H. S.; Choi S. G.; Park H.-H.; Rozenberg M. J., A new route to the Mott-Hubbard metal-insulator transition: Strong correlations effects in $Pr_{0.7}Ca_{0.3}MnO_3$, Sci. Rep., 2013, 3, 1704-1708.
(20) Dubost, V.; Cren, T.; Vaju, C.; Cario, L.; Corraze, B.; Janod, E.; Debontridder, F.; Roditchev, D. Resistive Switching at the Nanoscale in the Mott Insulator Compound $GaTa_4Se_8$, Nano Lett., 2013, 13, 3648-3653.
(21) Querré, M.; Janod, E.; Cario, L.; Tranchant, J.; Corraze, B.; Bouquet, V.; Deputier, S.; Cordier, S.; Guilloux-Viry, M.; Besland, M.-P. Metal–Insulator Transitions in $(V_{1-x}Cr_x)_2O_3$ Thin Films Deposited by Reactive Direct Current Magnetron Co-Sputtering, Thin Sol. Films, 2016, 617, 56-62.
(22) Rupp, J. A. J.; Corraze, B.; Besland, M.-P.; Cario, L.; Tranchant, J.; Wouters, D. J.; Waser, R.; Janod, E. Control of Stoichiometry and Morphology in Polycrystalline V_2O_3 Thin Films Using Oxygen Buffers, J. Mater. Sci., 2020, 55 (30), 14717-14727.
(23) Caneiro, A.; Bavdaz, P.; Fouletier, J.; Abriata, J. P. Adaptation of an Electrochemical System for Measurement and Regulation of Oxygen Partial Pressure to a Symmetrical Thermogravimetric Analysis System Developed Using a Cahn 1000 Electrobalance, Rev. Sci. Instr., 1998, 53, 1072-1075.
(24) Petricek V., Dusek M., Palatinus L., JANA 2006; Academy of Science of Czeck Republic: Praha, 2006.
(25) Makuła, P.; Pacia, M.; Macyk, W. How to correctly the band gap energy of modified semiconductor photocatalysts based on UV–Vis spectra, J. Phys. Chem. Lett., 2018, 9, 6814–6817.
(26) Oyama, T.; Iimura, Y.; Takeuchi, K.; Ishii, T. Synthesis of $(Cr_{1-x}V_x)_2O_3$ Fine Particles by a Laser-Induced Vapor-Phase Reaction and Their Crystal Structure. J. Mat. Sci., 1999, 34, 439-444.
(27) Vegard, L. Die Konstitution der Mischkristalle und die Raumfullung der Atome, Z. Physik, 1921, 5, 17-26.
(28) Tatsuyama, C.; Fan, H. Y. Raman Scattering and Phase Transitions in V_2O_3 and $(V_{1-x}Cr_x)_2O_3$, Phys. Rev. B, 1980, 21, 2977-2983.
(29) Shim, S.-H.; Duffy, T. S.; Jeanloz, R.; Yoo, C.-S.; Iota, V. Raman Spectroscopy and X-Ray Diffraction of Phase Transitions in Cr_2O_3 to 61 GPa, Phys. Rev. B, 2004, 69, 1441-(07-24).
(30) Yang, H.; Sladek, R. J.; Lattice-Dynamical Model for the Elastic Constants and Raman Frequencies in $(V_{1-x}Cr_x)_2O_3$, Phys. Rev. B, 1985, 32, 6634–6643.
(31) Guo, Y.; Clark, S. J.; Robertson, J. Calculation of Metallic and Insulating Phases of V_2O_3 by Hybrid Density Functionals, J. Chem. Phys., 2014, 140, 054702-054706.
(32) Austin, I. G.; Turner, C. E. The Nature of the Metallic State in V_2O_3 and Related Oxides, Phil. Mag., 1969, 19, 939-949.
(33) Le, H.-L. T.; Goniakowski, J.; Noguera, C. Properties of Mixed Transition Metal Oxides: M-M′-O_3 in Corundum-Type Structures (M, M ′ = Al, Ti, V, Cr and Fe), Phys. Rev. Mat., 2018, 2, 085001-085010.

(34) McWhan, D. B.; Rice, T. M.; Remeika, J. P. Mott Transition in Cr-Doped V_2O_3, Phys. Rev. Lett., 1969, 23, 1384-1387.
(35) Reid, A. F.; Sabine, T. M.; Wheeler, D. A. Neutron Diffraction and Other Studies of Magnetic Ordering in Phases Based on Cr_2O_3, V_2O_3 and Ti_2O_3, J. Sol. Sta. Chem., 1972, 4, 400-409.
(36) Mashiko H.; Oshima T.; Ohtomo A., Band-gap narrowing in α-$(Cr_xFe_{1-x})_2O_3$ solid-solution films, Appl. Phys. Lett., 2011, 99, 241904.

For Table of Content Only

Graphic for Manuscript

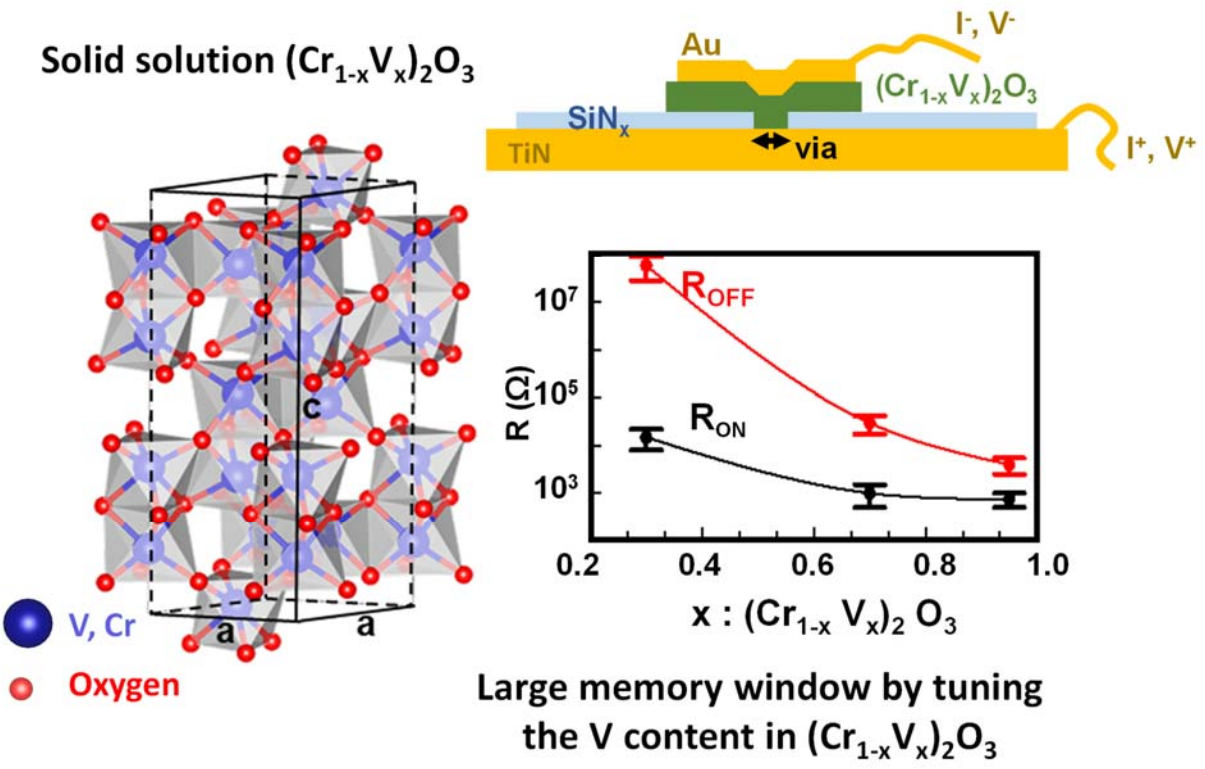

Large memory window by tuning the V content in $(Cr_{1-x}V_x)_2O_3$